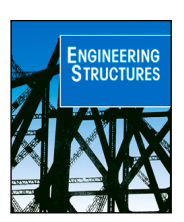
ELSEVIER

Contents lists available at ScienceDirect

Engineering Structures

journal homepage: www.elsevier.com/locate/engstruct





Mechanical performance of polyhedral hollow glass units under compression

Joseph Robert Yost ^a, Mohammad Bolhassani ^b, Philipp Amir Chhadeh ^c, Liam Ryan ^a, Jens Schneider ^c, Masoud Akbarzadeh ^{d,*}

- a Structural Engineering Teaching and Research Laboratory (SETRL), Villanova University, Villanova, PA, United States of America
- ^b The Bernard and Anne Spitzer School of Architecture, The City College of New York, NY, United States of America
- c Institute of Structural Mechanics and Design, Technische Universität Darmstadt, Darmstadt, Germany
- d Polyhedral Structures Laboratory, Department of Architecture, Weitzman School of Design, University of Pennsylvania, Philadelphia, PA, United States of America

ARTICLE INFO

Keywords: Hollow glass unit Compression-dominant glass structures Polyhedral glass structures 3D/polyhedral graphic statics

ABSTRACT

This research presents an experimental program and a numerical analysis executed to understand the strength and stiffness properties of polyhedral hollow glass units (HGU) that are intended for use in modular construction of all-glass, compression-dominant, shell type structures. The proposed compression-dominant geometric form has been developed using the form finding methods of 3D/polyhedral graphical statics. This research takes the first steps towards a new construction methodology for glass structures by exploiting the high compression strength of glass. The test matrix includes four HGUs, two each fabricated with 1 mm and 2 mm thick adhesive tape where the glass plates are all 10 mm thick annealed float glass cut using a 5-axis abrasive waterjet. Testing was done with the HGU oriented such that load was introduced on the short side edges of the two deck plates, resulting in an asymmetric load-support condition. All samples failed explosively by flexural buckling. Strain and deformation data clearly show the presence of second order behavior resulting from bending deformation. In general, linear axial behavior transitions to nonlinear second order behavior, with increasing rates in deflection and strain growth ultimately ending in glass fracture on the tension surfaces of the buckled deck plates. Failure resulted in complete disintegration of the deck plates, but with no observable cracking in any of the side plates and a secure connection on all adhesive tape. A companion finite element analysis was performed to validate the experimental results of this study. The results of the experimental and numerical programs clearly demonstrate the feasibility of using HGUs for modular construction of compression-dominant, all-glass shell type structures.

1. Introduction

Funicular structural forms maximize the structural performance and minimize the use of materials and resources. These systems carry applied loads in the form of pure tensile/compressive axial forces such that the form/geometry of the structure matches its internal flow of forces. The Sagrada Familia by Antoni Gaudí is an excellent example of using such forms in design and engineering. Gaudí used tedious physical form-finding techniques to find such funicular forms for his breathtaking structures. However, many eminent engineers and designers such as Guastavino, Maillart, Eiffel, Nervi relied on geometric methods of structural design, known as Graphical Statics, to design their efficient structures. Graphical Statics (GS) methods represent a group of powerful and intuitive geometric techniques for form-finding and analysis that originated in the pre-digital era and continue to be used and developed even today [1–8].

In GS-based methods, equilibrium of forces is represented by a geometric entity called the *force* diagram. Structural geometry or force flow in response to applied loads together with support reactions is called the *form* diagram. In two-dimensional graphic statics, that has been practiced since 1860, equilibrium of each structural node or thrust network is represented by a closed polygon of forces. Each edge of the force polygon is parallel (or perpendicular depending on the design convention) to an edge connected to a node in the form diagram. Consequently, the force magnitude in each member of the form is equivalent to the length of its corresponding edge in the force polygon.

This geometric relationship between equilibrium of forces and structural form render form-finding methods quite intuitive and explicit. For instance, the force diagram of compression-only forms consists of closed, convex force polygons, therefore, finding compression-only

E-mail addresses: joseph.yost@villanova.edu (J.R. Yost), mbolhassani@ccny.cuny.edu (M. Bolhassani), chhadeh@ismd.tu-darmstadt.de (P.A. Chhadeh), lryan17@villanova.edu (L. Ryan), schneider@ismd.tu-darmstadt.de (J. Schneider), masouda@design.upenn.edu (M. Akbarzadeh).

^{*} Corresponding author.

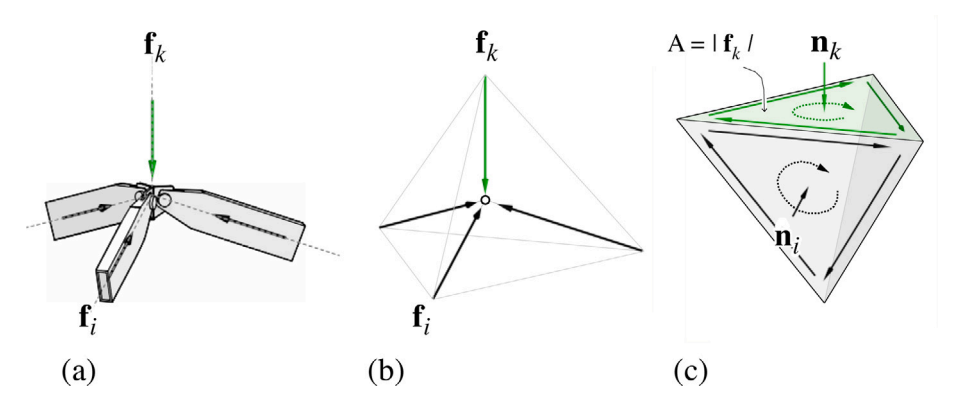


Fig. 1. (a) A 3D structural joint with an applied force and internal forces in its members; (b) the form diagram/bar-node representation of the same joint in the context of 3DGS; and (c) the dual reciprocal force diagram consisting of planar faces where each face is normal to a member in the joint, and the area of the face represents the magnitude of the force in the member.

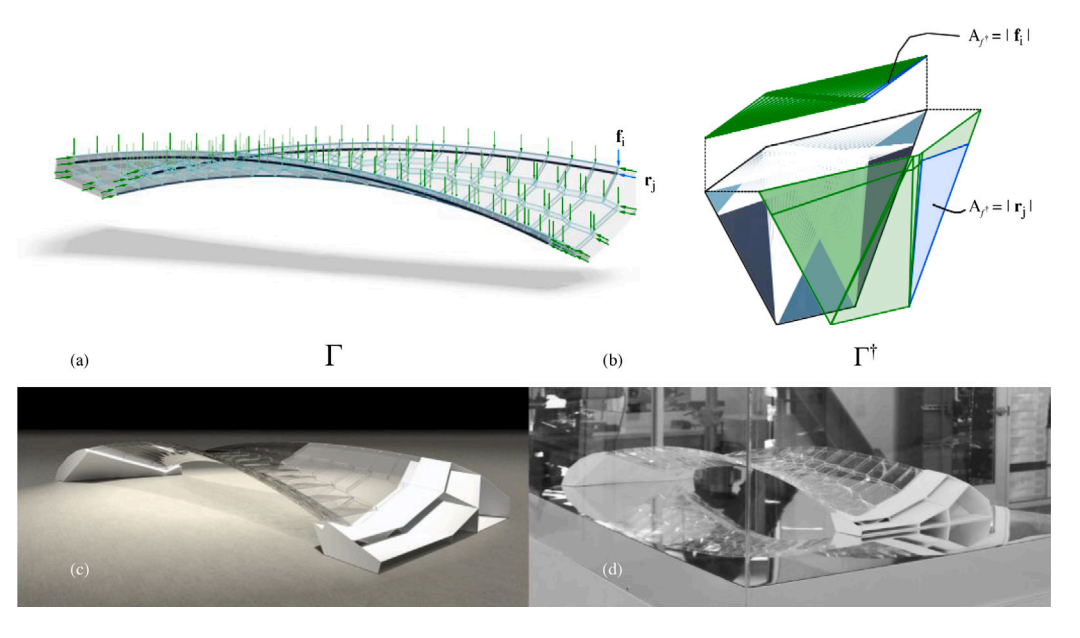


Fig. 2. (a) The form (Γ) and its force (Γ^{\dagger}) diagram of the bridge developed by using 3D graphic statics and PolyFrame plugin [14,17]; (c) a visualization of the conceptual design of the bridge; and (d) a physical scale model made of thin acrylic sheets (Courtesy of Polyhedral Structures Laboratory).

funicular forms is quite intuitive using GS-based methods [5,9]. Structures designed by GS-based methods are among the best examples of innovative and efficient use of materials. Gustave Eiffel's tower, Maillart's Salginatobel bridge, Guastavino's ultra-thin load-bearing vaults with only two layers of tile brick are all designed using GS-based methods [10–12].

3D graphic statics Using Reciprocal Polyhedral Diagrams

Despite its clear strength and advantages, traditional graphical statics were limited to 2D diagrams, and a designer could only design 2D abstraction of three-dimensional structures. In 2016, the methods of 2DGS were extended to 3D based on a 150-year-old proposition by [13] in Philosophical Magazine [7,8,14–16]. In 3D graphic statics (3DGS), equilibrium of external forces or a single node of an equilibrated structure is represented by a closed *polyhedron* or a polyhedral *cell* with planar faces. Each face of the force polyhedron is perpendicular to an edge in the form diagram, and the magnitude of the force in the corresponding edge is equal to the area of the face in the force polyhedron (Fig. 1). Employing methods 3DGS in structural design expands the horizon of interaction between form and function to the realm of unexplored efficient spatial structural forms.

Compression-only glass structure: motivation and objectives

Using 3DGS methods in structural form finding results in lightweight structures with high-performance structural behavior [18-20]. Moreover, the resulting structural forms are polyhedral geometries with planar faces. Therefore, not only does 3DGS find efficient structural forms, but its planarity constraint facilitates construction using flat sheet materials as is conceptually shown in Fig. 2. To take advantage of the planar geometry of the reciprocal polyhedral diagrams in construction, this research will explore the structural efficiency and behavior of a lightweight, ultra-transparent glass pedestrian bridge constructed out of planar glass sheets in compression. The ultimate objective of this research is to: (a) design and build a compression-dominant glass pedestrian bridge constructed mainly of flat sheets of glass, and (b) revisit conventional structural glass detailing to extend existing techniques for the future of efficient construction with glass. For this purpose, an allglass pedestrian bridge was designed using the methods of 3DGS in a compression-only form by aggregating convex polyhedral cells [14,21]. PolyFrame beta [22] plugin for Rhinoceros software [23] was used to generate structural form and the corresponding force diagram for the compression-dominant design. The compression-dominant form of the bridge consists of planar faces in a double-layer configuration with vertical faces connecting the top and bottom layers of the structure as

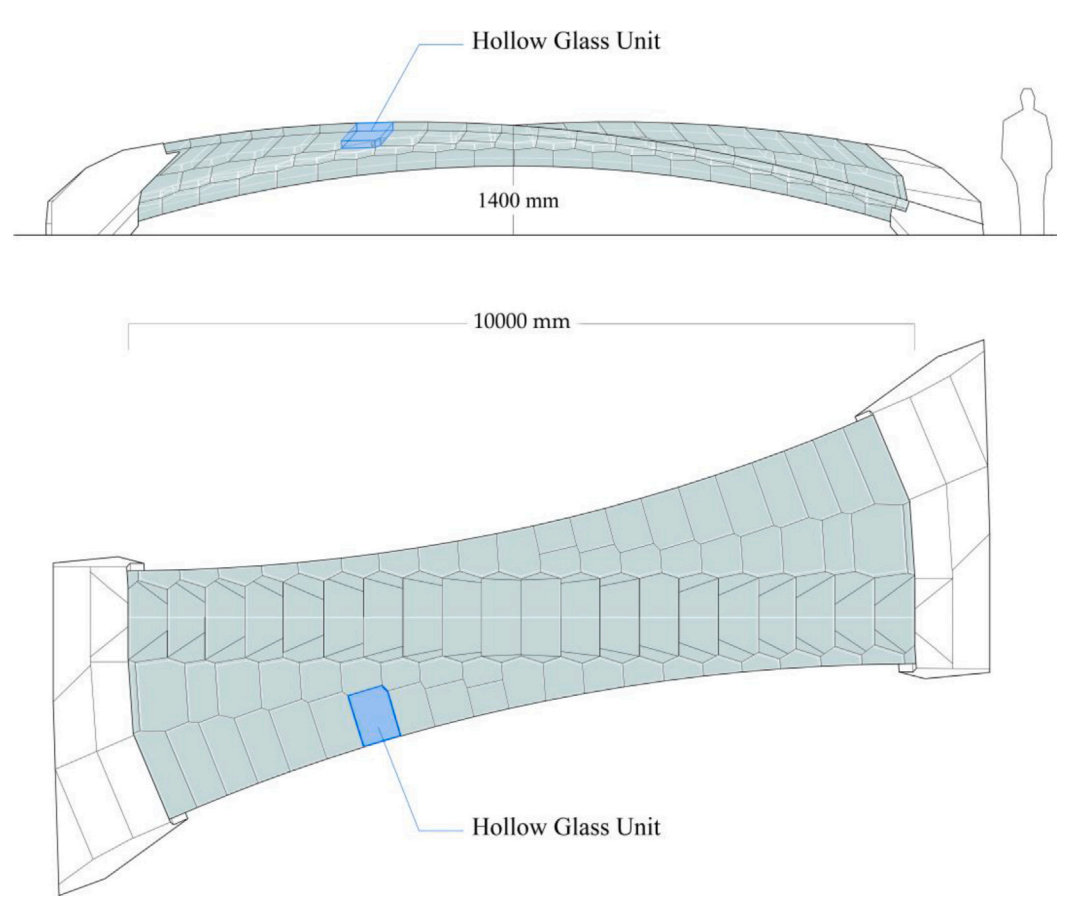


Fig. 3. Plan and elevation of proposed glass bridge highlighting a Hollow Glass Unit as the fundamental building element of the structure (Courtesy of PSL).

shown in Fig. 2a. Bridge geometry consists of interconnected closed convex polyhedral cells as shown in Fig. 3. Thus, it is proposed to construct the bridge as an assembly of Hollow Glass Units (HGU), which is inherited from the polyhedral geometry of the bridge. The HGUs will aggregate in a compression-dominant configuration to complete the form of the bridge.

All Glass Systems: Literature Review

The use of glass for load bearing structural elements in compression is logical given the material's high compression strength and stiffness. Exploiting this potential will, however, require careful attention to controlling load path through geometric form and appropriate connection detailing so that failure limit states other than those associated with the material's compression strength are not dominant. Many examples of signature glass structures exist throughout the world and include among many the National Grand Theater in China [24], the Aldar Headquarters in Abu Dhabi [25], the Louvre Pyramid in Paris France [26], and the Louis Vuitton Foundation museum, also in Paris France [27]. However, strength and stiffness of these structures are dependent on steel or concrete framing, with glass serving the central architectural role, but a secondary structural function. European standards, such as the German DIN 18008, only allow load bearing of glass in an out-ofplane direction, for i.e., snow and wind loads (DIN 18008). Currently, there is no formal allowance in standards for in-plane loads acting on glass. Consequently, the number of structures that use glass as the primary load-bearing element are quite limited [28,29].

The ultimate aspiration of this research is to unite the architectural and structural functions of glass through modular assembly of HGUs into a compression dominant structural form. New and emerging technologies such as 3D printing, additive manufacturing, waterjet cutting, and generative design will make possible efficient structural

form minimizing use of material and associated fabrication of complex geometry [30–36]. Precedent for this vision currently exists. For example, the Great Court at the British Museum canopy required the assembly of 4878 hollow rods, 1566 connector nodes and 3312 glass plates, each part with a unique geometry. Furthermore, construction of the Golden Terraces in Warsaw Poland was made with 7123 hollow steel sections, 2300 nodes and 4780 glass panels, again each with unique geometry. The Strasbourg Train Station extension is noted for its use of double curved bent glass, of nearly 6000 $\rm m^2$ in total, supported by steel arches [37–39].

The cited structures are significant, demonstrating the frontiers of glass construction, but still relying on steel as an integral component of the structural system. A significant challenge with an all-glass structure is addressing the transfer of force between neighboring HGUs, which will require detailing the connection with an interface material. The interface material should be transparent and have the necessary stiffness and hardness to resist high bearing stress and simultaneously resist local cracking associated with stress concentrations. Importantly, the property of transparency is not related to function, but rather related to the bridge's aesthetic and maintaining the transparent quality of the proposed structural system. Research related to this need is available from [40,41] and is related to development of a cast-glass modular structural system. The research shows hardness and tear resistance are the most important parameters for the interface material.

2. Research scope and objective

The proposed modular all-glass structural system consists of an assembly of interlocking three dimensional HGUs that are arranged geometrically into a compression-dominate configuration. Therefore, the system strength and stiffness are essentially the aggregate of the individual parts, or HGUs. It is therefore necessary to know the unit

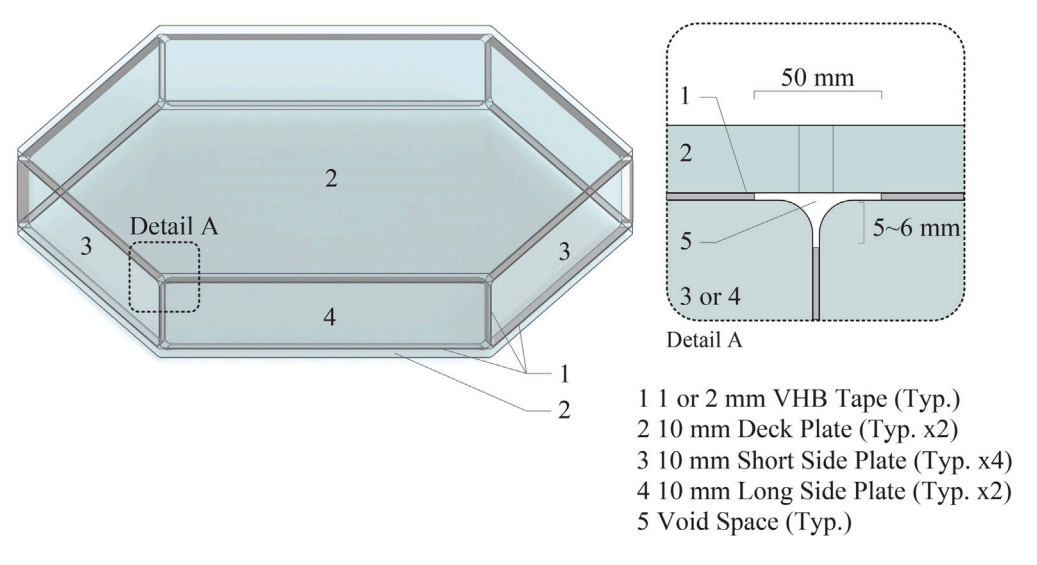


Fig. 4. Typical HGU components.

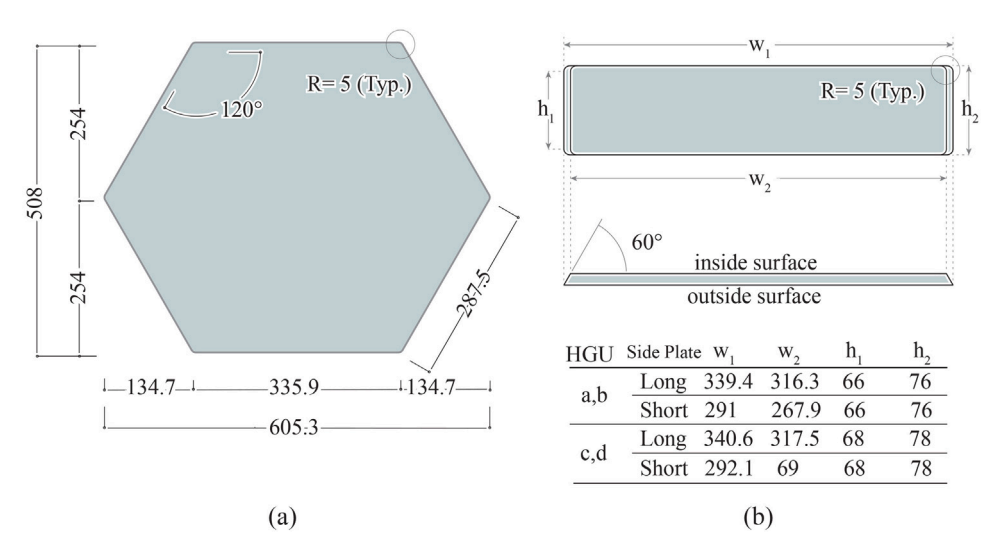


Fig. 5. HGU component geometry (a) Deck plate, (b) Side plate (the dimensions are in mm).

behavior so that the system behavior can be understood. The scope of this research study is experimental and numerical investigation of an individual HGU loaded in axial compression. The objectives include understanding force—deformation and linear vs. nonlinear response, failure mode and ultimate strength, and integrity of the connections between individual glass plates that collectively represent an individual HGU.

3. Sample details and assembly methodology

A total of four HGU samples were fabricated for testing and designated HGUa, HGUb, HGUc, and HGUd. Each HGU sample had the shape of an elongated hexagonal prism consisting of two deck plates, and two long and four short side plates, as is shown in Fig. 4. All plates were 10 mm (3/8 in) thick soda-lime annealed glass, and all connections were made using $3M^{\rm TM}$ Very High Bond (VHB) Tape [42]. VHB tape is a family of double sided foam tapes made with an acrylic adhesive and manufactured using closed cell technology. The particular tape used was transparent, had a thickness of either 1 or 2 mm, and a corresponding width of 19 or 12 mm, respectively. Samples HGUa and HGUb were assembled using 2 mm thick VHB tape (tape ID VHB 4918f), and samples HGUc and HGUd were assembled using

1 mm thick VHB tape (tape ID VHB 4910). Tape properties from the manufacturer are given in Table 1.

Individual plate geometric details are shown in Fig. 5, where it is noted that all corners were rounded with a 5 mm radius fillet and the short dimension of all side plates (long and short) were beveled at 60° to match the 120° deck plate corner angle. As a consequence of the 5 mm corner fillet, the VHB tape on the short dimension of the side plate was terminated at approximately the point of fillet tangency. Furthermore, to accommodate assembly of the HGU, VHB tape applied to the long dimension of all side plates was terminated 25 mm from the projected end of the glass. This resulted in a void space at all corners where the deck and side plates meet of approximately 50 mm by 5 mm, as is shown Detail A of Fig. 4. In shaping the glass to the geometry of Fig. 5 all cutting was done using a 5-axis abrasive waterjet with a cut edge surface texture corresponding this technology.

The first step in the assembly process involved cleaning and priming all glass surfaces where VHB tape was to be applied. This was done as recommended by the tape manufacturer to improve bond performance. First the glass bonding surface was cleaned using a 50% water 50% isopropyl alcohol solution, and this was followed by priming using $3M^{\rm TM}$ Silane Glass Treatment AP115. For both cleaning and priming a lint free cloth was used.

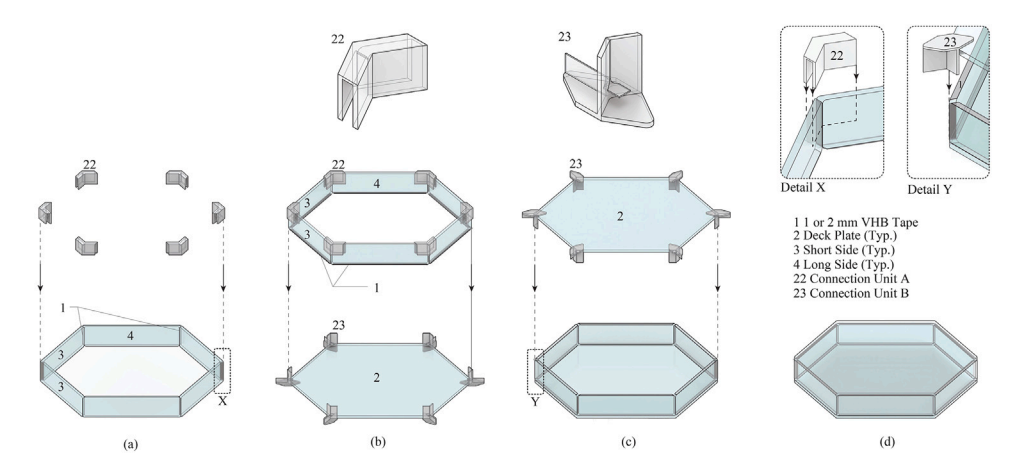


Fig. 6. HGU Assembly (a) Assembly of side wall hexagon; (b) Placement of first deck plate; (c) Placement of second deck plate; (d) Fully assembled HGU.

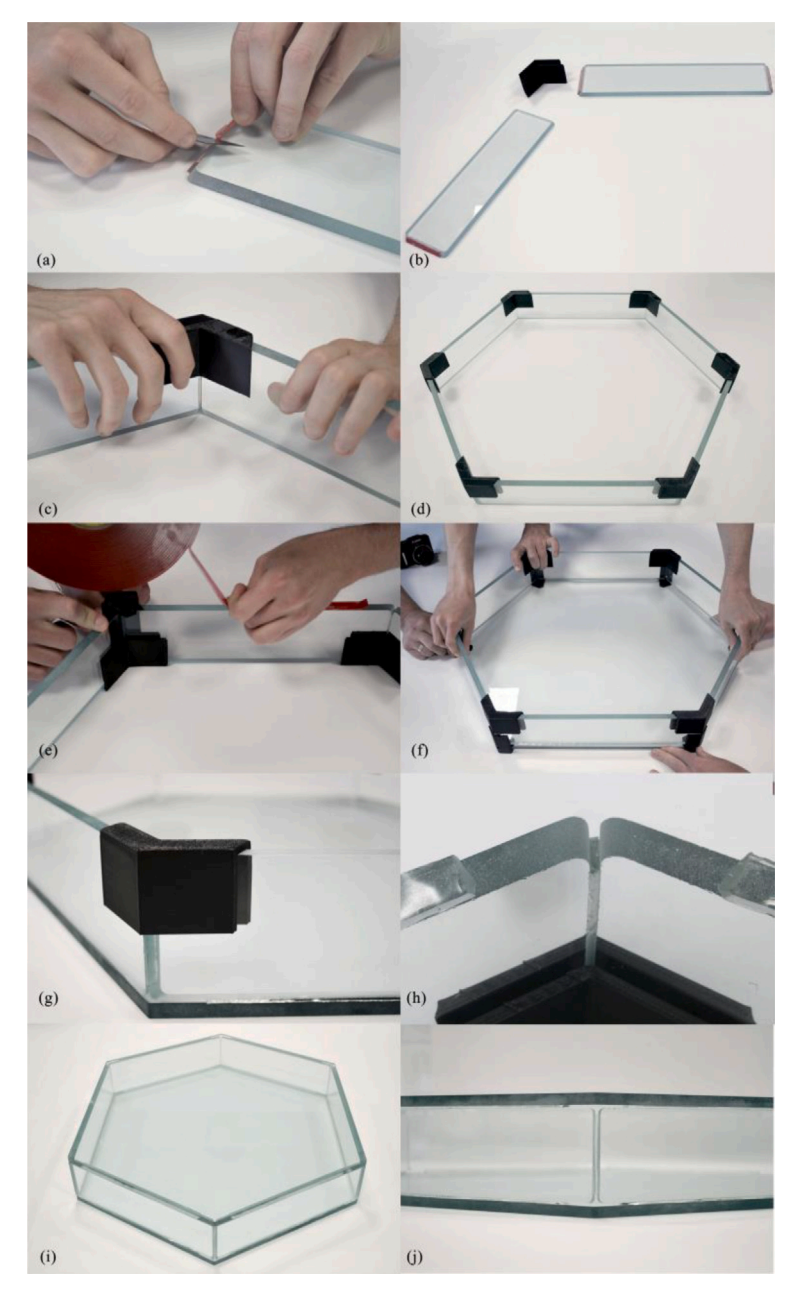


Fig. 7. (a)-(j): Assembly process and the sample HGU for the load testing with 2 mm VHB tape.

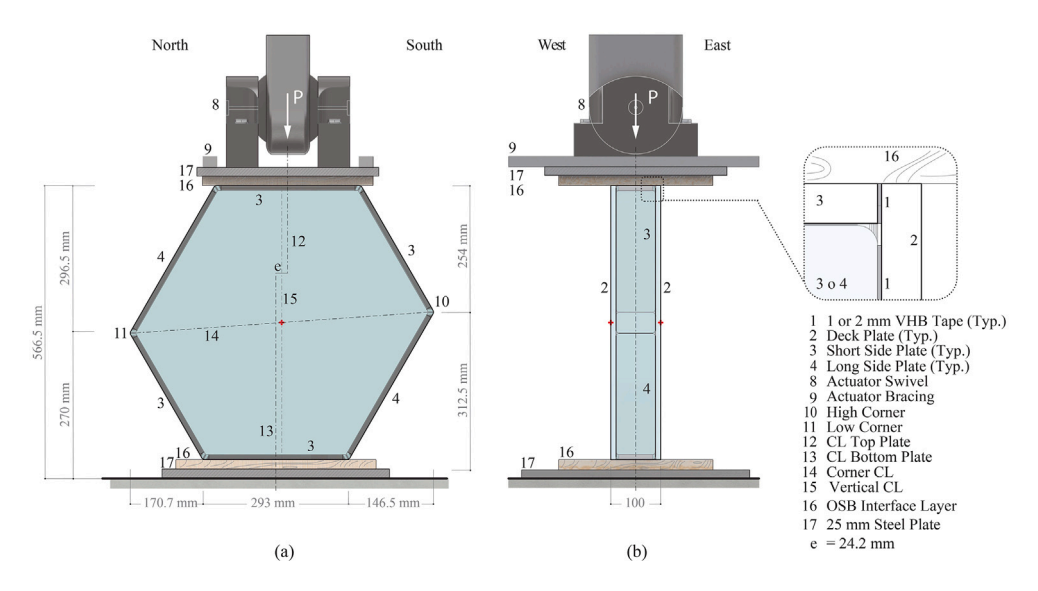


Fig. 8. Experimental load and support: (a) Elevation looking East; and (b) elevation looking North.

Table 1
VHB tape properties reported by the manufacturer [42].

Tape ID	Thickness (mm)	Width (mm)	90 peel adhesion	Static shear at 22 °C	Dynamic overlap shear
VHB 4910	1	19	26 N/cm	1000 g	480 kPa
VHB 4918f	2	12			

The ensuing assembly of a typical *HGU* is shown in Figs. 6 and 7, and started with connecting one long side plate with two short side plates, producing a three-side-plate-unit. During this step the VHB tape was first applied to the short dimensions of the long side plate, with one tape side bonded to the glass bevel and the other side still with the protective covering. At this point the width dimension of the tape was trimmed using a razor blade to match the thickness of the glass bevel (Fig. 7a). The protective foil was then removed and the two short side plates were bonded using a recommended pressure of about 100 kPa, which was applied manually. Special connection clips were 3D printed out of PLA (Polylactic acid) to true the assembly to the required geometric tolerance, designated Connection Unit A (CUA) in Figs. 6 and 7. With two of these three-side-plate-units assembled, they were each joined together forming a side-wall hexagon (Figs. 6a and 7d).

This was followed by attachment of the first deck plate, which is shown in Fig. 6b. First VHB tape was applied to the long dimension of all side plates and the tape width dimension trimmed using a razor blade to match the glass thickness. Then 3D printed Connection Units B (CUB) were placed on all corners of the deck plate, again to ensure the required assembled geometric tolerance. The side-wall hexagon was then lowered down through the connection units B and onto the deck plate (Fig. 6b and Fig. 7f). Pressure was then manually applied to the recommended 100 kPa. Placement of the second deck plate started with placement of the VHB tape on the top surface of the side-wall hexagon, shown in Figs. 6c and 7e. As before, prior to removal of the tape's protective covering, the tape width was trimmed to match the glass thickness with a razor blade. Connection Units B were then fitted to the deck plate corners and the second deck plate was lowered and bonded to the VHB tape, as is shown in Fig. 6c. Lastly, the Connection Units B were removed completing the assembly process. It should be noted, that the HGU corner void space of Fig. 4 Detail A and Fig. 7j is a consequence of the tabs that secure CUB to the deck plate. Photo of a fully assembled HGU are shown in Figs. 7i and 7j.

4. Experimental program

4.1. Load and support

As mentioned, two of the four HGU samples were assembled using 2 mm VHB tape, designated HGUa and HGUb, and two samples were assembled with 1 mm VHB tape, designated HGUc and HGUd. All four samples were tested with the HGU positioned vertically and with load applied to the centerline of the top HGU short side, as is shown in Fig. 8a. The consequence of this asymmetric orientation is a north-south eccentricity (e) between top and bottom centerlines of 2.42 cm (see Fig. 8a). This asymmetric load case was intentionally selected as being more critical than a symmetric orientation where the HGU would be loaded and supported on the two long sides.

Load was applied through a 2.5 cm steel plate bolted to the actuator swivel and in contact with an interface layer. The interface layer was used to prevent direct contact between steel and glass. 10 mm thick oriented strand board (OSB) was selected as the interface material to prevent local cracking of the deck plate glass on the loaded edge due to high stress concentration. A similar support detail was used on the bottom short side, with a 10 mm OSB interface layer used between the HGU and a 2.5 cm steel plate grouted to the laboratory floor. The test was run in displacement control at a rate of 0.25 mm/min. It should also be noted that applied load is assumed to act on the deck plates only, and not the short side plates at the load and support locations. This is a consequence of the negligible shear stiffness of the VHB tape connecting the deck and side plates.

It is noted there is no out-of-plane force applied to the HGU, as would be associated with pedestrian live load. It is proposed that in the actual bridge pedestrian live load follow a gravity load path that delivers these forces to the HGU perimeter, and not directly to the HGU deck plate. This would involve live load applied to laminated heat-treated glass designed specifically for bending. This glass surface would then frame into the HGU perimeter creating the in-plane only load condition for the HGU experimental program.

During testing of the first sample, HGUa, the actuator capacity of 165 kN was achieved with no failure. Consequently, the sample was unloaded and a new actuator with capacity 600 kN was used to retest sample HGUa, and the remaining three samples. In presenting the test results, the first and second tests of HGUa are referred to as $HGUa_1$ (unfailed) and $HGUa_2$ (to failure), respectively.

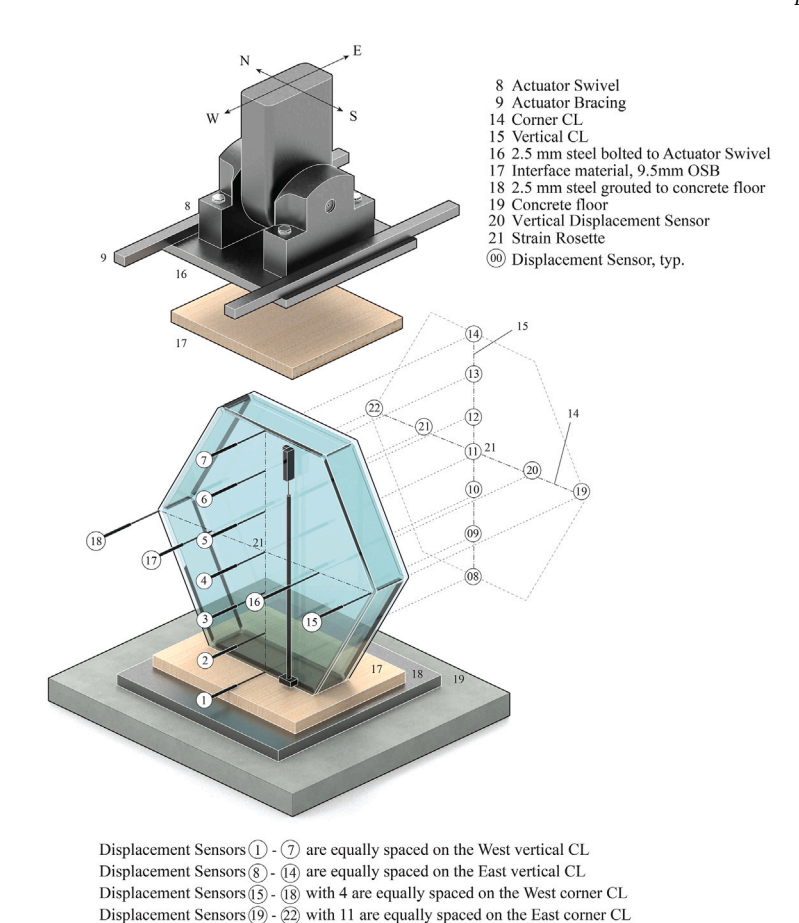


Fig. 9. Instrumentation plan.

4.2. Instrumentation and data acquisition

The instrumentation plan is shown in Fig. 9 and includes displacement and strain measurement. As can be seen, seven displacement sensors were equally spaced between top and bottom on the HGU vertical centerline, and on each the east and west deck plates. These sensors, designated 1-to -7 west and 8-to -11 east, measured horizontal displacement or displacement perpendicular to the plane of the deck plates. It is noted that sensors 4 and 11 are located at the deck plate centroid on the west and east sides, respectively. Horizontal displacement was also measured on the corner centerline by equally spaced sensors 15-to -18 with 4 west and 19-to -22 with 11 east. Additionally, a 0-45-90 degree strain rosette was located at the intersection of the vertical and corner centerlines and on the outside surface of each the east and west deck plates. The strain rosette was oriented with the 90 degree gauge on the vertical centerline. All test data was collected by a 16 bit data acquisition system at a rate of 25 Hz. A photo of the complete test setup is given in Fig. 10.

4.3. Test results

Center deck plate deflection

Shown in Fig. 11a are load vs. deck plate out-of-plane displacements for HGUa and HGUb (2 mm VHB tape) measured on the vertical centerline at mid-height on each the east- (E) and west-sides (W) sides (i.e sensors 4 and 11 in Fig. 9), and again in Fig. 11b for Samples HGUc and HGUd (1 mm VHB tape). Note that displacement is positive for 'push' on the sensor, and negative for 'pull'. Also, as mentioned, Sample HGUa experienced two tests, designated test $HGUa_1$ to 165 kN, which represents the actuator capacity, and then unloaded, and a second test, $HGUa_2$, with a new actuator and reloaded to failure.

From Fig. 11, it is seen that both deck plates (east and west) are displacing in the same direction with one side in 'push' and the other in 'pull'. Thus, each deck plate is buckling in the same direction, and for samples HGUa (a_1 and a_2), HGUb and HGUc this is towards the west (i.e. west is in push) and for HGUd this is towards the east (i.e. east in push). Also, the load–displacement behavior for all samples is approximately symmetric which would suggest equal load distribution to each the east and west deck plates, and equal edge restraint on all sides with the VHB tape.

All samples were loaded to failure which occurred suddenly by flexural buckling. Importantly, the OSB interface layer was completely effective in preventing any local cracking on the load and support edges of the deck plates. Failure was sudden and explosive, with ejection of deck plate glass in the direction of buckling. There was no cracking of any side plates (short and long) as can best be determined from post test visual observation, and there was no debonding of the VHB tape from either deck plate or side plate glass. A typical photo at maximum load (HGUb) is shown in Fig. 12a. This was followed immediately by formation of a deck plate crack (Fig. 12b) and explosion of the deck plate material to the west (Fig. 12c). A post failure photo can be seen in Fig. 12d with shattered deck plates and uncracked side plates. Load at failure for $HGUa_2$ and HGUb (2 mm VHB) was 165 and 185 kN, respectively, with an average of 175 kN, and for samples HGUc and HGUd (1 mm VHB) failure occurred at 186 and 202 kN, respectively, with an average of 194 kN.

From Fig. 11, the force–deformation response can be generalized as first approximately linear with a low deflection rate. This is followed by a transition to a nonlinear response with increasing deflection rate, which is associated with axial force eccentricity and second order behavior. For tests $HGUa_1$ and $HGUa_2$, this transition is rather gradual occurring at about 130 kN and 90 kN, respectively. For these samples

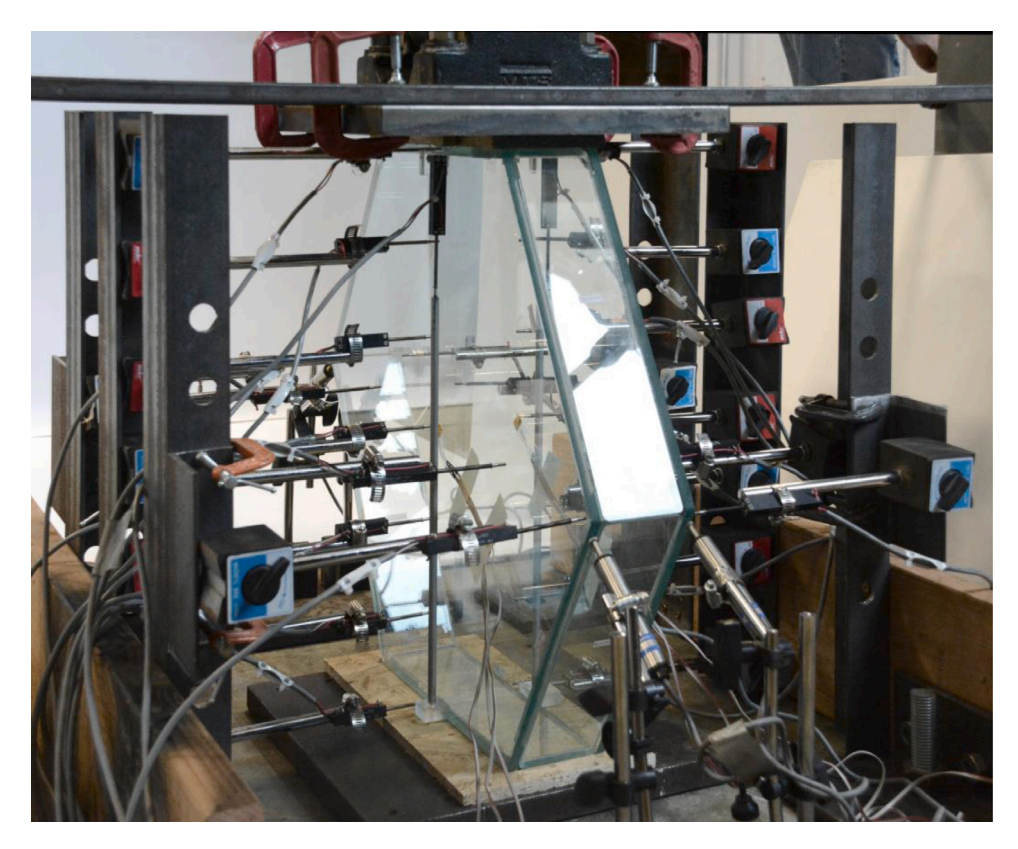


Fig. 10. Photo of test setup.

at maximum load, there is still a measurable deflection rate. For sample HGUb, this transition is much more abrupt occurring at about 150 kN, and at failure, the load–deflection response is essentially flat. HGUc, like HGUa, experiences a gradual transition to a nonlinear response at about 130 kN, and like HGUb, has an essentially flat load–deflection response at failure. Sample HGUd experienced negligible deflection until about 180 kN at which point there was a rapid transition to nonlinear behavior. This continues to a maximum load of 202 kN and corresponding deflection of 2.1 mm. This is followed by a descending deflection rate to failure at about 198 kN and an average deflection of about 4.8 mm. It should be noted that this was a displacement control test and, hence, a negative displacement rate (i.e. increasing deflection under decreasing load) is possible, and this would not be possible for a load control test.

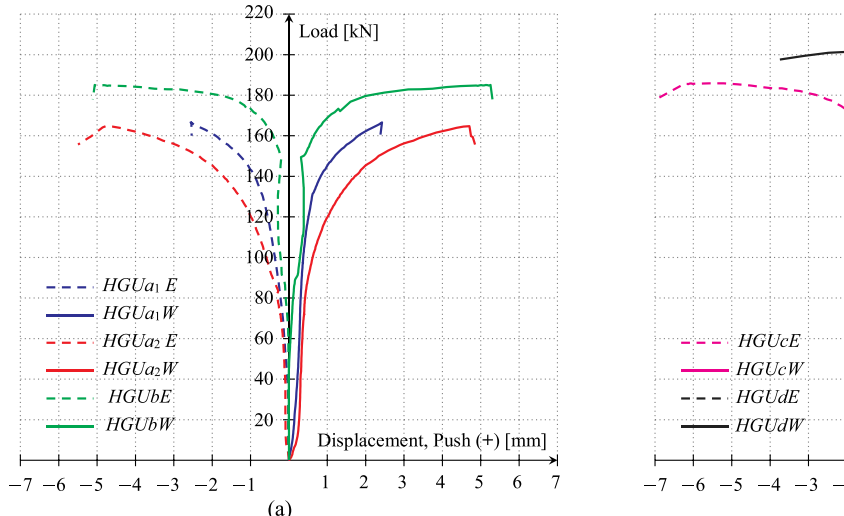
From the results of Fig. 11a,b, there is no obvious correlation between VHB tape thickness (1 and 2 mm) and corresponding load-deflection response and ultimate strength. In general, the variability observed in test behavior can be associated with minor variations in each test setup. Most notably the variation related to initial load eccentricity in the east–west direction will accelerate the onset of second order nonlinear behavior. By this measure, initial east–west load eccentricity from lowest to highest test is HGUd, HGUb, HGUc and $HGUa_2$.

Center deck plate strain and principal stress in the glass surface

Measured strain in the vertical direction on the outside surface at the geometric center of the east and west deck plates are shown in Fig. 13. From these data, the east and west strains are initially approximately equal and increase linearly in compression with increase in load. The strain increase during this phase is in response to increasing axial load. For the 2 mm thick VHB samples $HGUa_2$ and HGUb, this axial dominate phase terminates at about 90 and 150 kN, respectively, and for the samples with 1 mm thick VHB tape, HGUc and HGUd, at about 130 and 180 kN, respectively. As load is further increased,

the east and west strains trend nonlinearly in different directions. This behavior reflects the presence of second order bending associated with axial force eccentricity that is in the same direction for both east and west deck plates. This is to be expected from the displacement results of Fig. 11, noting that vertical strain associated with second order bending will be tension and compression on the outside surfaces of the push and pull sides, respectively. From Fig. 11a and b it is seen that the push deck plate is west for $HGUa_1$, a_2 , b, and c and east for HGUd. For samples $HGUa_1$, $HGUa_2$ and HGUc, the onset of bending is gradual, as is noted by the smooth and gradual change in strain rate for both tension and compression. A very different response is noted for samples HGUband HGUd, where a sharp inflection in strain rate is noted reflecting a sudden increase in force eccentricity and corresponding lateral deck displacement. This is consistent by the deflection results of Fig. 11. At failure, the strains on the outside surface of the push deck plates are all well in tension and range between 310 (HGUa2) and 540 microstrain (HGUc). On the pull side strains range in compression between -1090 $(HGUa_2)$ and -1200 microstrain (HGUc).

The acquired strain rosette data is next used to determine the principal stresses on the outer fiber at the deck plate centroid using a plane stress transformation together with material properties for glass as Young's Modulus of E = 70 GPa, and Poisson's Ratio of ν = 0.22. The maximum principal stresses are taken for tension on the push side plate (i.e. west for $HGUa_1$, $HGUaa_2$, HGUab and HGUac, east for HGUd), and for compression, on the pull side deck plate (i.e. opposite side). These results are shown in Fig. 14a and b for tension and compression, respectively. As noted, in tension, all principal stresses follow a similar bi-linear pattern where they are initially relatively linear and tightly banded together. This is followed by a sharp inflection and transition to a relatively flat response where stress increases significantly under negligible force increase. This nearly bi-linear response ends at failure where the principal tensile stresses for samples $HGUa_2$, HGUb, HGUc and HGUd are calculated to be 24.7, 31.1, 42.4 and 39 MPa, respectively. Given the magnitude of these maximum principal tensile



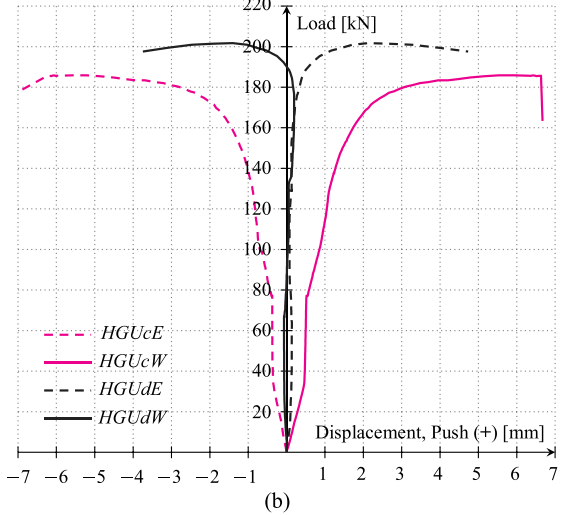


Fig. 11. Load vs. center deck plate displacement: (a) HGUa₁, a₂ and HGUb (2 mm VHB); and (b) HGUc and HGUd (1 mm VHB).

stresses, it would be expected that failure was initiated by cracking associated with flexural tension stress on the extreme fiber of the deck plate. However, it is also observed from Figs. 12b and e that the first crack is believed to have formed at the free edge of the deck plate and was likely initiated by surface irregularities associated with waterjet cutting, which would significantly reduce crack resistance. Thus, bending tensile stress at this location was sufficient to initiate cracking and failure. Identification of the crack formation region was beyond the scope of this study and will be investigated in future research. Thus, for the purpose of numerical discussion, the correlation between cracking, strength and tensile stress is considered at the location of strain measurement. Finally, from Fig. 14b, the minimum principal stresses (i.e. compression) have a very different response, showing a linear portion that gradually transitions to a nonlinear response. There is then gradual and continual acceleration in stress rate until failure. The principal compression stress at failure for samples $HGUa_2$, HGUb, HGUc and HGUd are calculated to be -72.5, -77.7, -86.7 and -78 MPa, respectively. From these results, the maximum principal compression-to-tension stress ratios at failure are 2.94, 2.48, 2.05, and 2.0 for samples $HGUa_2$, HGUb, HGUc and HGUd, respectively.

Deflection profile

Referring to Fig. 9, for each the east and west deck plates there are seven displacement sensors equally spaced on the vertical centerline. Deformation from these sensors plotted at a given load will show the deflection profile and this deformation represents bending associated with elastic flexural buckling. Deflection profiles on the vertical centerline are shown in Fig. 15 at maximum load and just before failure occurred. As can be seen, both deck plates always buckled in the same direction. Both 2 mm samples buckled towards the west, and for the 1 mm samples HGUc and HGUd buckled towards the west and east, respectively. For all samples the shape of the deflection profile is as expected for buckling of a pin ended compression member with single curvature, zero end moment, maximum deformation at mid-height and an approximately symmetric profile about a horizontal axis through mid-height of the HGU. For samples $HGUa_2$, b and c the deflection profiles of the east and west deck plates are approximately the same. For sample HGUd, however, the east deck plate experienced greater lateral deformation than the west deck plate by about 20 percent. Normalizing the lateral deformation as the ratio of HGU height (566.5 mm) to maximum lateral deflection for samples $HGUa_2$, b, c and d yields 120, 109, 85, and 106, respectively. These ratios are relatively low considering the tensile-brittle nature of float glass. Furthermore, the deflection profile of Fig. 15 correlates with the

strain distribution trends of Fig. 13. That is deformation towards the west $(HGUa_2, b, c)$ induces tension and compression bending stress on the outside surfaces of the west and east deck plates, respectively. For deformation to the east (HGUd), the opposite is true. The shape of the vertical strains shown in Fig. 13 are consistent with this behavior and represent the superposition of axial and bending strain, with the bending part dominant near failure.

5. Numerical modeling

5.1. Overview and modeling methodology

With the use of ANSYS Workbench, the HGU experimental tests have been modeled using the finite element (FE) method. In the FE model, the hexagonal HGU was loaded with north-south eccentricity as shown in Fig. 8. The HGU model consists of two deck plates and six side plates. These plates are connected using strips of VHB tape. Based on the experimental program it has been shown that there is no bond failure between the VHB tape and glass due to the applied axial load. Therefore, in the FE model a tie connection between the VHB tape and glass was selected and a cohesive material failure assumed. In the tie connection, displacement compatibility between neighboring VHB and glass nodes is employed. From the experimental program, the OSB was used to avoid local stress concentrations on the loaded glass edge that could lead to premature fracturing (See Table 2 for material properties). This favors a HGU deck plate buckling failure and consequently increases the HGU load bearing capacity. The material properties of the VHB tape are taken from internal testing performed at the Technische Universität Darmstadt, and are shown in Table 2 together with the material properties of glass and OSB. Glass properties are taken from DIN [43] as typical for float glass. The OSB properties were determined by trial and error to match experimental load-deformation results. The iterative procedure for determining the material properties of OSB results in a softer behavior than literature values for OSB would indicate. These softer material properties are intended to simulate the plastic deformation that is caused by the plowing of the deck plates into the OSB without using a complex material model. Furthermore, material properties available in the literature apply to OSB in bending or used as a wall element. However, in the case of HGU testing, the OSB is subjected to a compression bearing force in the out of plane direction. In this application there is no bending and correspondingly the available material properties to not apply. To minimize computational time, an isotropic-elastic material was used for both VHB and OSB. It is understood that VHB is a hyperelastic material

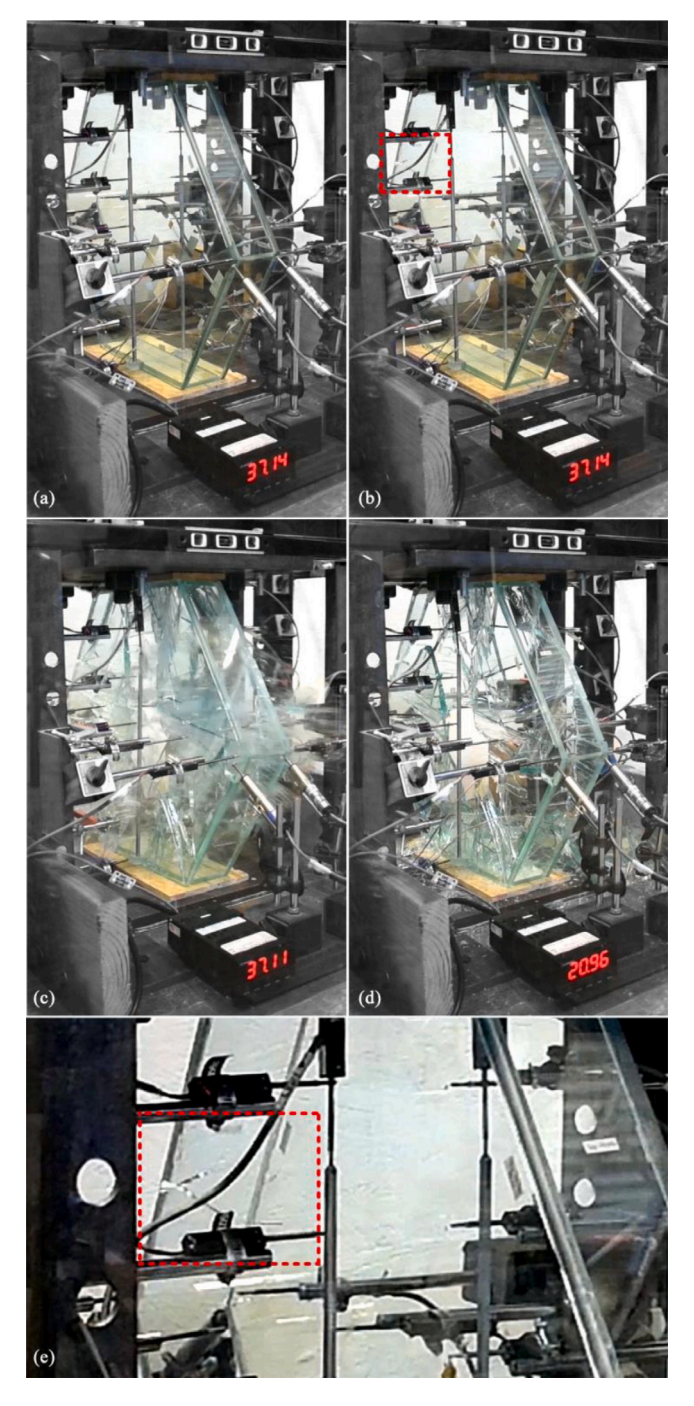


Fig. 12. (a) A moment before formation of any crack; (b) the formation of the first crack; (c) failure stage; and (d) the crushed sample (37 kips is the loading); (e) the magnified region highlighted in (b) where the first visible crack is formed, but the crack formation study was beyond the scope of this paper.

and OSB is orthotropic, however, FE analyses were run with these material models and a simple isotropic-elastic model and no significant difference was found in the results.

The HGU geometry for the FE model was created by importing a CAD file from Rhinoceros 3D into ANSYS Workbench and the following assumptions are made: Meshing of the individual glass and VHB tape components used the 'Multizone' method with hexahedral continuum elements. These elements are particularly well suited for problems in solid mechanics. The final element size is shown in Fig. 16 and was determined by means of a mesh refinement study.

In representing the glass-VHB tape interface, three models are available in ANSYS [44] for modeling contact problems. These are; a) node–node, b) node–surface and c) surface–surface connections. The

Table 2 Material properties used in the material model.

Material ^a	Modulus of elasticity (MPa)	Shear modulus (MPa)	Poisson's ratio
Glass	70,000	28,690	0.22
VHB-Tape ^b	1.79	0.6	0.49
OSB	325	125	0.3

 $^{^{\}rm a}\text{All}$ materials are assumed to be isotropic elastic.

latter is particularly well suited for typical engineering applications where both the source and target components of the contact represent

^bThe number is valid for room temperature.

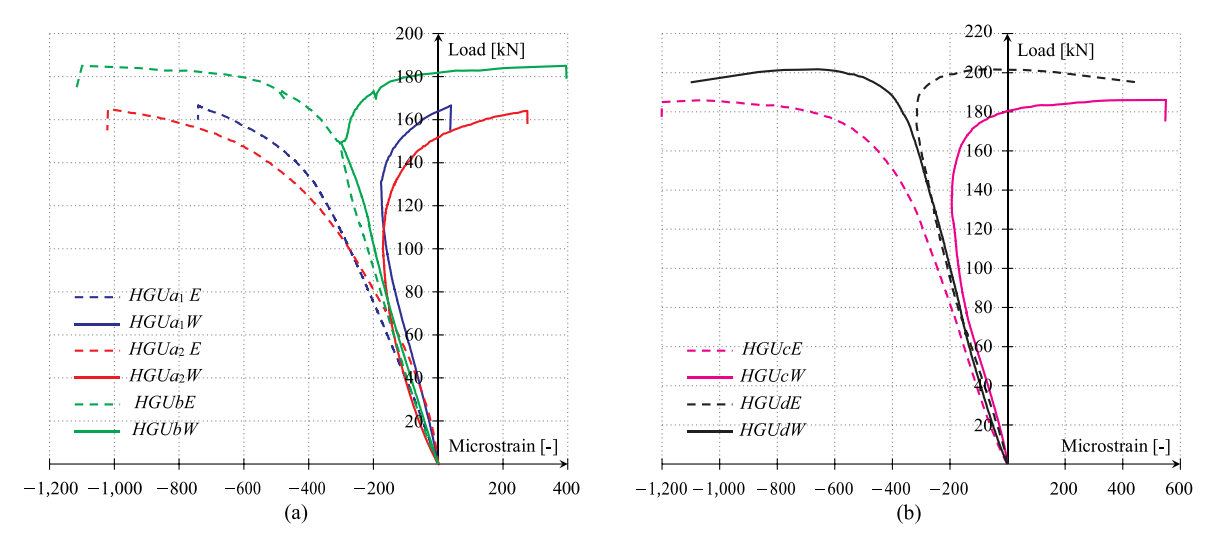


Fig. 13. Load vs. center deck plate vertical strain: (a) HGUa₁, a₂ and HGUb (2 mm VHB); and (b) HGUc and HGUd (1 mm VHB).

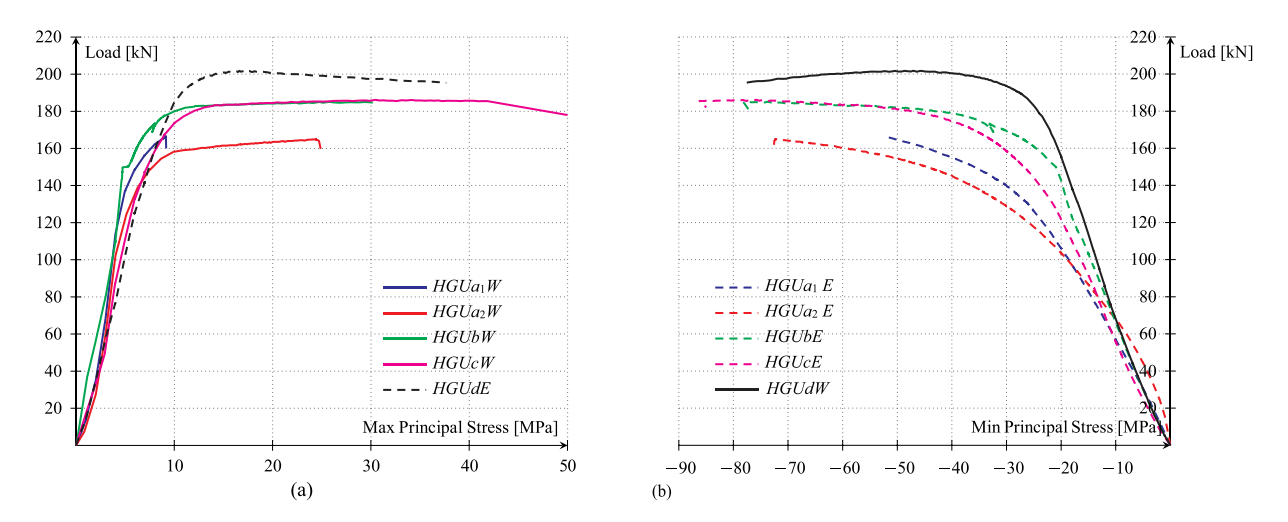
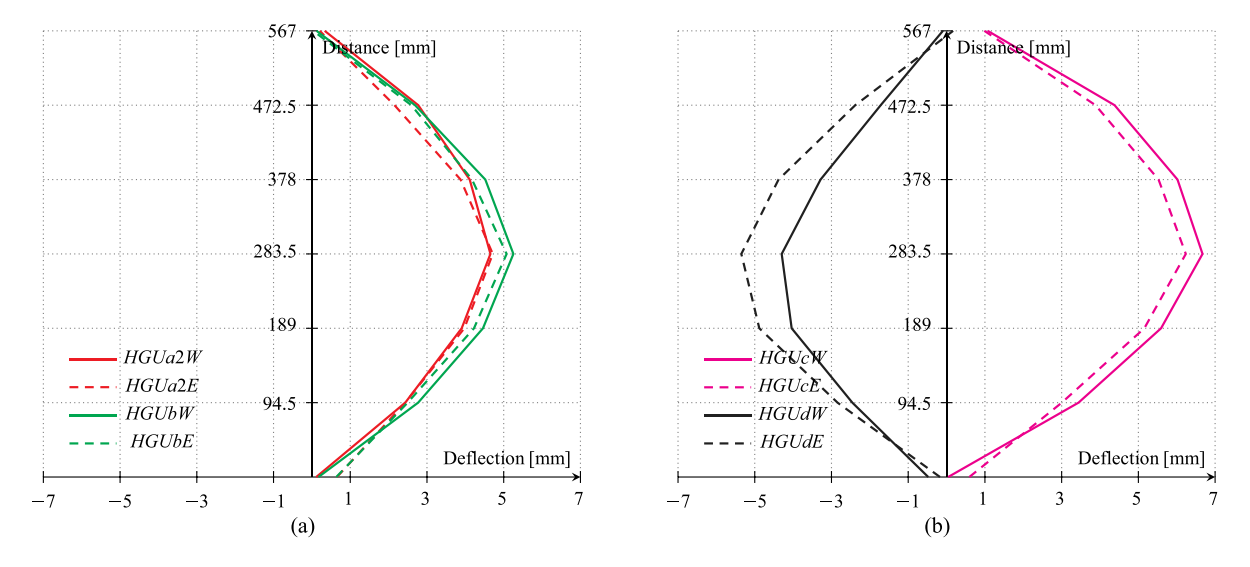


Fig. 14. Load vs. center deck plate principal stress: (a) Maximum principal stress and (b) Minimum principal stress.



 $\textbf{Fig. 15.} \ \ \text{Deflection profile at maximum load vs. distance along the vertical center line: (a) samples \ \textit{HGUa}_2 \ \text{and } \ \textit{HGUb}; \ \text{and (b) samples } \ \textit{HGUc} \ \text{and } \ \textit{HGUd}.$

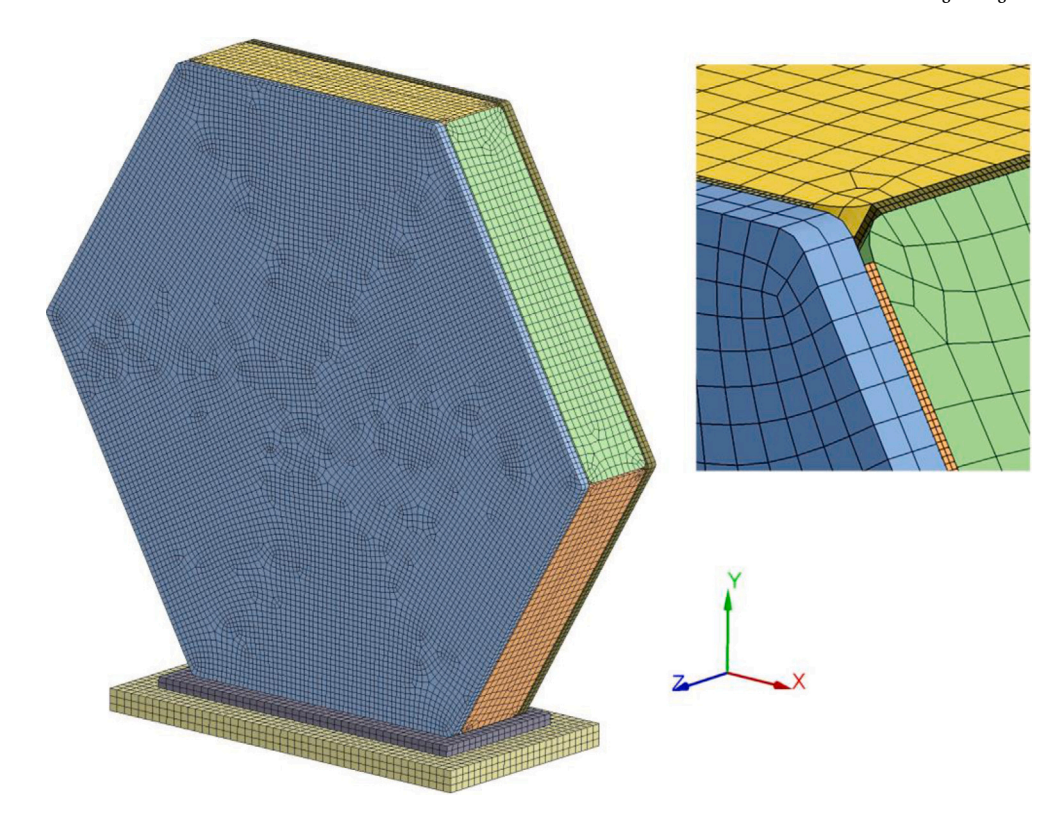


Fig. 16. Final mesh resolution (OSB top load plate not shown for clarity).

a surface and not individual points or edges. For this reason, the surface–surface contact model was used to represent the glass–tape interface.

5.2. Analysis procedure

A non-linear analysis was performed by an applied displacement of 0.25 mm/min, the same as in the experimental program. In the non-linear analysis, large deformation is activated in ANSYS Workbench where the program continuously updates the nodal coordinates as the solution converges to the final deformed configuration [44]. As mentioned, in developing Young's modulus for the OSB interface material a trial and error approach was used to reproduce the experimental force–deformation results.

An eigenvalue buckling analysis was used to calculate the HGU buckling strength and is based on the Euler Buckling solution. For complex structures, however, the buckling strength according to Euler is usually not reached in an actual compression member due to imperfections and non-linearities. To better simulate these conditions, a second order analysis was used where equilibrium is established based on the deformed shape of the structure due to the previously defined buckling shape. Gradually increasing the load, taking into account the large deformations and second order geometric non-linearities, allows determination of the critical load at which the system becomes unstable.

The procedure of non-linear buckling analysis consists of three consecutive steps. First, a small static axial force is applied to the model. In this case a force of $1000\ N$ was applied to the upper OSB plate nodes. Next, the eigenvalue buckling analysis is performed by ANSYS in which the load from the previous analysis is increased stepwise until the load level at which local buckling occurs is achieved. In this procedure, ANSYS determines the failure for different buckling failure modes. The lowest load level is the critical mode. The load level calculated by ANSYS is $225\ KN$. At this load, the deckplates start to buckle. Finally, in the third step a further static analysis is performed

where the model setup is simulated according to the test setup. The outside surface of the bottom OSB plate is modeled as pin supported, and the outside surface of the top OSB plate is modeled as roller supported with displacement release in the loading direction. Load was applied by displacing the OSB load plate top surface nodes at a rate of 0.25 mm/min. Furthermore, a perturbation load from the eigenvalue buckling analysis is applied. The perturbation load is a fraction of the deformation from the critical buckling mode to ensure the system is deforming according to the buckling failure mode.

5.3. Numerical results

Numerical results are shown in Fig. 17 as force–deformation response, Fig. 18 as deformation perpendicular to the plane of the deck plate at the Eigenvalue buckling load and Fig. 19 as maximum principal stress at the Eigenvalue buckling load. It can be seen from the force–deformation results of Fig. 17 that there is a flexural buckling condition when the Eigenvalue buckling load level is reached. Furthermore, the numerical response is approximately bilinear which is similar to the experimental test results, in particular for sample HGUd. It is also noted that the HGU experimental strength is less than predicted by numerical modeling. This can be related to the fact that experimental failure is instantaneous and related to cracking resulting from tension associated with second order bending, and the FE model as developed cannot capture the behavior of glass cracking.

This can be related to the formation of micro-cracks and their growth in the deck plates as a results of tension in plane direction from the applied load causing failure, and the FE model as developed cannot capture the behavior of glass cracking.

In comparing the load–displacement curves of the experimental test results and the numerical analysis one can see that finding a best fit is only possible to a limited extent (see Fig. 17). This is because the numerical model does not represent exactly the experimental conditions of the HGU tests. Most notably in this regard is going to be experimental error related to locating the applied actuator load located

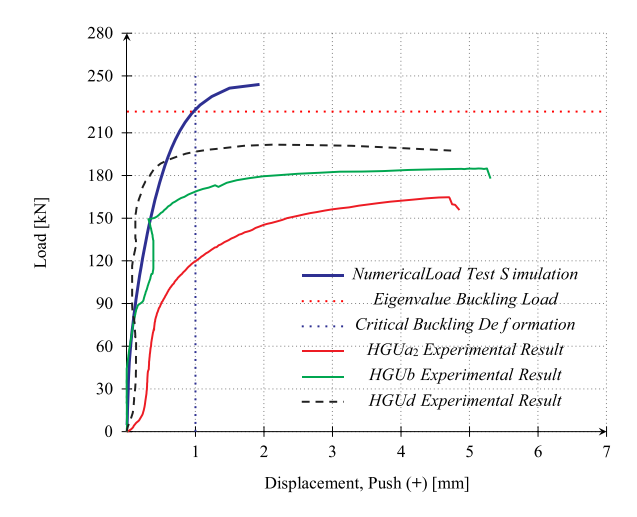


Fig. 17. Comparison of experimental and numerical load vs. out-of-plane deck plate displacement.

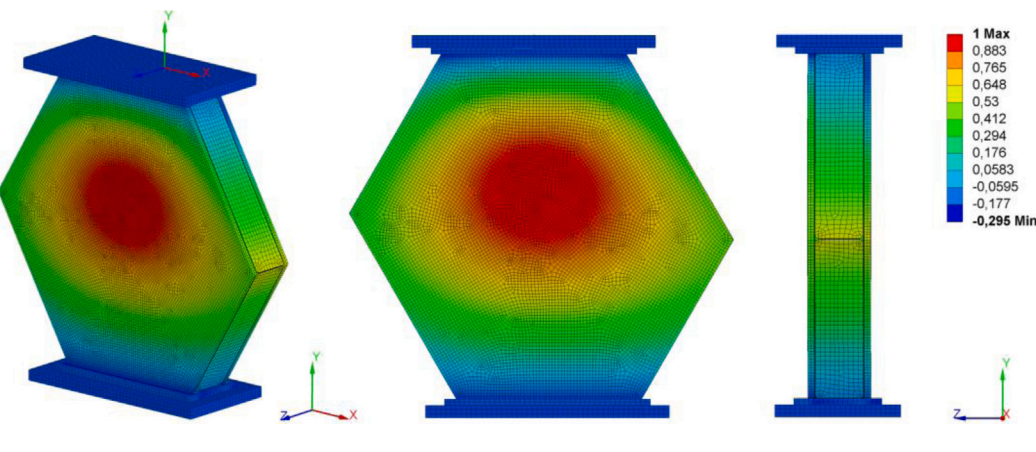


Fig. 18. Deformation at Eigenvalue buckling load.

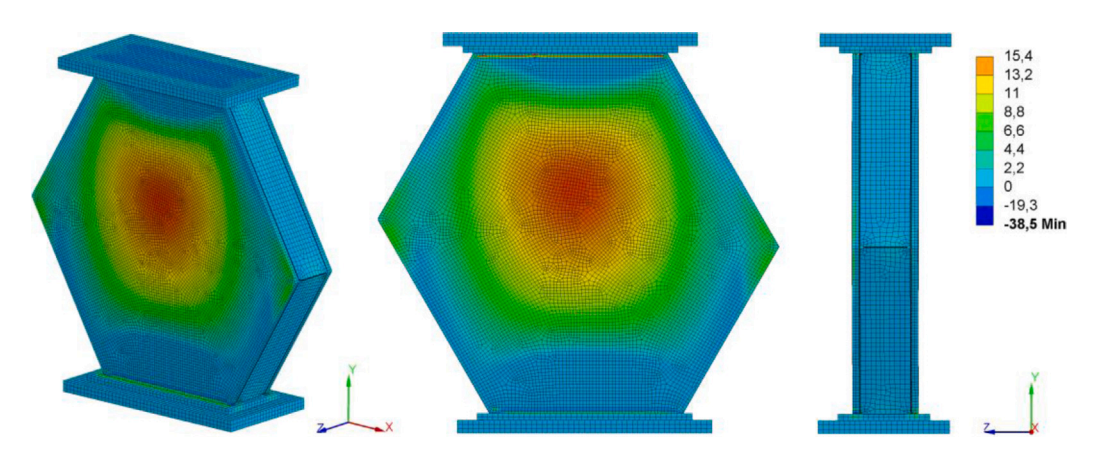


Fig. 19. Principle stress at Eigenvalue buckling load.

directly at the centroid of the top HGU short side plate in the east–west direction. In reality there is force eccentricity in the east–west direction of experimental test setup that is not included in the geometry of the FE model. This initial experimental east–west force eccentricity will result in the onset of nonlinear behavior much sooner than predicted by numerical modeling. This is clearly seen in the experimental results where there is a distribution in the load at which the onset on nonlinear behavior occurs. Other sources of error might include imperfect bonding of VHB tape, nominal rotational restraint at the load and support locations, initial out of straightness of the deck plates, and actual glass

thickness. Although, it is understood that the main error source is initial east—west eccentricity of applied load.

In Fig. 18 it can be seen that the deck plates bulge in an out-of-plane direction. This is a consequence of second order flexural bending and corresponding axial force eccentricity. Also, the pinned restraint top and bottom is noted, as is curvature of the deck plate buckling deformation. Referring to the maximum principal stress field shown in Fig. 19 the distribution reflects a dishing type plate deformation with bending about two axes. This behavior is consistent with the deck plate buckling deformations observed in Fig. 18.

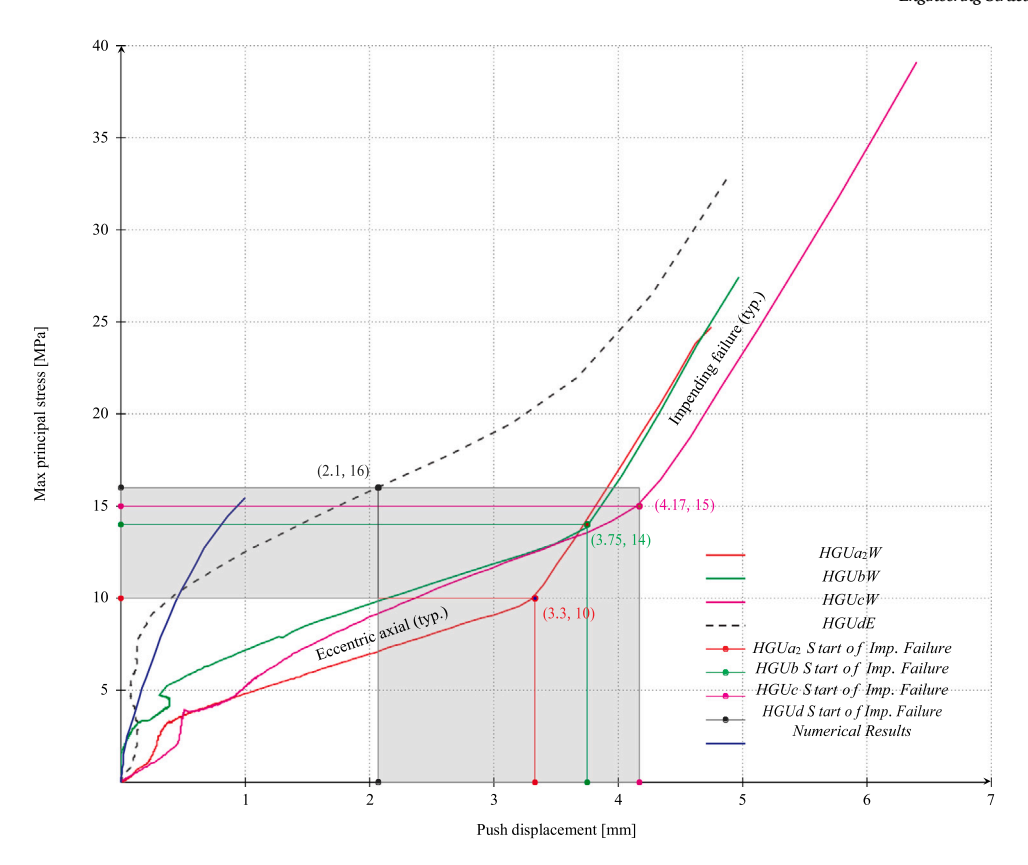


Fig. 20. Push displacement vs. principal tensile stress at geometric centroid of deck plate.

Considering the above mentioned sources of error, the numerical results are in reasonably good agreement with experimental data, and, again, this is particularly true for test HGUd. The FE method is reasonably accurate in capturing the initial linear elastic axial dominant part of the experimental tests. However, the numerical results in Fig. 17 show that the specimen reaches a load plateau at 240 kN which is 17% higher than the experimental results for HGUd (202 kN). However, the Eigenvalue buckling analysis found the HGU shows buckling in one of the deckplates at 225 kN (dashed-line) which results in impending failure of the structure. The HGU still transfers load from the actuator to the bottom support due to alternative load paths until the deformation in the structures exceeds the limits of convergence. Furthermore, the HGU experimental load capacity should be less than the numerical analysis Eigenvalue buckling strength. This was discussed earlier and is related to the brittle properties of glass and corresponding cracking associated with flexural buckling. Finally, the numerical analysis shows that the onset of HGU flexural buckling can be defined when the deck plate out-of-plane deformation reaches 1 mm and, correspondingly, the maximum deck plate principal tensile stress is 15.4 MPa.

6. Results interpretation and limit state discussion

Experimental and numerical results provide a response history that can serve as a reference for derivation of a strength design criterion specific to the limit state of flexural buckling. Important in this context is correlating the response history to a design methodology that safely accounts for the entirety of the HGU's physical response to applied axial load. This physical response can be broadly characterized as three main regions: axial, eccentric axial, and impending failure. Ultimately failure occurs at the end of impending failure and is a consequence of tensile fracture on the extreme fiber that results from buckling deformation and second order bending. In regard to the aforementioned regions, the region of impending failure is characterized by negligible

force increase and significant deformation and stress increase. Consequently, the failure limit state is defined at the end of eccentric axial region and beginning of impending failure region.

It is proposed that the strength limit state be defined using a limiting principal tensile stress (PTS) or deflection, the magnitude of which is related to that associated with the start of impending failure. Interaction between experimental PTS and corresponding push displacement is given in Fig. 20. For samples HGUa2, HGUb and HGUc the data shows an initial region of low deformation followed by an approximately bilinear response. These data regions correlate to the characteristic regions of axial, eccentric axial and impending failure, respectively. Accordingly, the coordinates corresponding to the onset of impending failure represent numerically the failure criteria related to PTS or deflection. For sample HGUd, the data clearly shows regions of axial and eccentric axial, however the impending failure region is defined by decreasing load. Therefore, for sample HGUd the beginning if impending failure is defined at maximum load. The coordinates at the beginning of impending failure are shown in Fig. 20 and range from 10 $(HGUa_2)$ to 16 MPa (HGUd) for PTS and 2.1 (HGUd) to 4.2 mm (HGUc) for displacement. Considering that stress is absolute in terms of its correlation to failure but displacement is relative, the proposed failure criterion for flexural buckling is a limiting PTS, and lower bounding the experimental data failure is defined to occur at a PTS of 10 MPa. It is noted that the numerical model results for PTS and deflection at the Eigenvalue buckling load were found to be 16 MPa and 1 mm, respectively. This point does fall within the experimental failure region limits as shown Fig. 20.

With 10 MPa PTS as a criterion for establishing the service limit state, the design methodology as either allowable stress design (ASD) or load and resistance factor design (LRFD) must be considered. With ASD, a simple factor of safety (FoS) is applied to the failure limit state to define the service limit state. Using LRFD methodology, the strength design philosophy is capacity must exceed demand, or the service limit state is correlated to the strength limit state using a combination of

statistical load factors (γ) and strength reduction factors (ϕ) . Furthermore, LRFD employs factors for ductility (η_D) and redundancy (η_R) to account for material behavior and load redistribution. Considering that the proposed system is for a pedestrian bridge, the load combination for dead (DL) and live (LL) load is initially considered. That said, the [45] LRFD strength design requirement is given as:

$$\phi R_n > \left\{ F_{DL} \gamma_{DL} + F_{LL} \gamma_{LL} \right\} \eta_D \eta_R
= F_{serv} \left\{ \%_{DL} \gamma_{DL} + \%_{LL} \gamma_{LL} \right\} \eta_D \eta_R$$
(1)

In Eq. (1) R_n is the nominal strength, ϕ is a strength reduction factor, F_{DL} , F_{LL} and F_{serv} are the dead, live and total service loads respectively, γ_{DL} and γ_{LL} are the dead and live load load-factors, respectively, η_D and η_R are ductility and redundancy factors, respectively, and \mathcal{C}_{DL} and \mathcal{C}_{LL} are the percentage of dead and live load relative to the total service load, respectively. From (1) the LRFD strength FoS can be determined as R_n/F_{serv} , or in terms of load, resistance, ductility and redundancy factors as:

$$FoS = \left\{ \%_{DL} \gamma_{DL} + \%_{LL} \gamma_{LL} \right\} \eta_D \eta_R / \phi \tag{2}$$

Assuming the service load is $50\%_{DL}$ and $50\%_{LL}$, and following the American Association of State and Highway Transportation Officials (AASHTO) LRFD methodology [45] which sets γ_{DL} = 1.25, γ_{LL} = 1.75, $\phi = 0.90$, and $\eta_D = \eta_R = 1.05$ the *LRFD* strength FoS is found by Eq. (2) as 1.84. For the sake of simplicity, consider the LRFD strength FoS as 2.0. Now, Eq. (1) is a strength criterion for design, and the proposed limit of 10 MPa is a PTS criterion. Experimental data is used to correlate 10 MPa PTS with a strength limit state in terms of force or capacity. Referring to the test data the load at 10 MPa ranges from 158 kN (HGUa2W) to 185 kN (HGUdE). Lower bounding the data establishes failure load at 158 kN, and using the LRFD strength FoS of 2.0, the service load is taken as 79 kN. The corresponding bearing stress on the loaded short side of the deck plate at the strength and service limit states is 30 MPa and 15 MPa, respectively. Next, the experimental factor of safety is determined as the ratio of maximum experimental load to 79 kN and is 2.09 and 2.34 for 2 mm VHB tape samples HGUa₂ and HGUb, respectively, and 2.35 and 2.56 for 1 mm VHB tape samples HGUc and HGUd, respectively. Consequently, the experimental FoS is between 5 and 30% greater than the proposed value of 2.0. This result is expected and is a consequence of lower bounding experimental strength corresponding to 10 MPa PTS.

In summary, using results from experimental testing the strength limit state is defined at a deck plate PTS of 10 MPa. This correlates to a capacity of 158 kN or, normalized in terms of bearing stress on the loaded side of the deck plate, 30 MPa. Using LRFD strength design methodology, a factor of safety of 2.0 is proposed, and the service load is suggested to be 79 kN. Finally, the experimental factor of safety is conservative relative to the proposed 2.0 and ranges between 2.09 and 2.56.

7. Conclusion

The research presented in this study is specific to axial loading of elongated hexagonal glass prisms, referred to as hollow glass units (HGU). It is proposed that large open space structures can be constructed as an assembly of interlocking HGUs arranged geometrically into a compression-dominate configuration using a three dimensional graphic statics method of analysis. An individual HGU is composed of two deck plates, four short side plates and two long side plates, all 10 mm thick float glass and connected with a double sided foam tape know as VHB. Four samples of identical geometry were tested, two made with 1 mm thick VHB tape and two made with 2 mm VHB tape. All samples were simply supported and monotonically loaded in displacement control. A companion finite element model was created in ANSYS Workbench. The following represents the conclusions and findings from the study.

- All samples failed in a flexural buckling mode with both deck plates displacing in the same direction. Failure was sudden and explosive, with shattered deck plate glass ejected in the direction of buckling displacement.
- Failure was a consequence of bending deformation related to flexural buckling and associated deck plate cracking resulting from tensile bending stress on the outer fiber of the deck plates. At failure the HGU height-to-maximum displacement ratio ranged from 85 to 120.
- It appears from photographic observation that cracking is likely initiated on the tensile fiber of the deck plate free edge. At this location crack resistance is expected to be reduced as a consequence of surface irregularities resulting from the waterjet cutting process.
- At failure the measured principal compression and tension stresses in the center of the deckplate ranged between -72.5 and -86.7 MPa, and 24.7 and 42.4 MPa, respectively.
- At failure there was no observable debonding between the glass and VHB tape, and all side plates remained in an uncracked condition.
- There was no significant difference in behavior or strength between samples constructed with 1 and 2 mm VHB tape.
- A simplified failure criterion of 10 MPa deck plate principal tensile stress is proposed. This failure criterion corresponds to the onset of impending failure, which is defined by rapid acceleration in deformation and strain at minimal increase in axial load.

The HGU flexural buckling strength is only achievable if local cracking on the loaded edge of the deck plate that is associated with micro stress concentrations is minimized. This will require use of an interface material that has the necessary properties of hardness and stiffness to smooth out bearing stresses at locations of local surface irregularity in the deck plate glass thickness. This was successfully accomplished in the experimental program with the use of OSB as an interface material between the load and support steel plates and HGU deck plate glass.

Declaration of competing interest

The authors declare that they have no known competing financial interests or personal relationships that could have appeared to influence the work reported in this paper.

Acknowledgments

This research was supported by University of Pennsylvania Research Foundation Grant (URF), United States, National Science Foundation CAREER AWARD, United States (NSF CAREER-1944691- CMMI) and the National Science Foundation Future Eco Manufacturing Research Grant, United States (NSF, FMRG-CMMI 2037097) to Dr. Masoud Akbarzadeh. Also, this study was supported by Villanova University Summer Grant Program (USG), United States to Dr. Joseph Yost. Special thanks to Zach Jones for his contribution to the figures of the paper. We are also grateful for the feedback received from Martien Teich at Seele Germany and Mr. Enrico Cutri and Mrs. Valerie Hayez at Dow, Switzerland. Special thanks to graduate student Cory Byrnes at Villanova University for his contribution in the assembly of the HGUs. In addition, we are also grateful for insights provided by Dr. Michael Drass at TU-Darmstadt.

References

- Maxwell J. On reciprocal figures and diagrams of forces. Philos Mag J Ser 1864;4(27):250-61.
- [2] Culmann K. Die graphische statik. Zürich: Verlag Meyer & Zeller; 1864.
- [3] Cremona L. Graphical statics: two treatises on the graphical calculus and reciprocal figures in graphical statics. Oxford: Clarendon Press; 1890.

- [4] Wolfe W. Graphical analysis: a text book on graphic statics. McGraw-Hill Book Company, Inc.; 1921.
- [5] Block P. Thrust network analysis: Exploring three-dimensional equilibrium. (Ph.D. thesis), Cambridge, MA, USA: MIT; 2009.
- [6] Fivet C, Zastavni D. Constraint-based graphic statics: New paradigms of computer-aided structural equilibrium design. J Int Assoc Shell Spatial Struct 2013:54(4):271–80.
- [7] Akbarzadeh M. 3D graphic statics using polyhedral reciprocal diagrams. (Ph.D. thesis). Zürich. Switzerland: ETH Zürich: 2016.
- [8] McRobie A. Maxwell and rankine reciprocal diagrams via Minkowski sums for 2d and 3D trusses under load. Int J Space Struct 2016;31:115–34.
- [9] Whiteley W, Ash P, Bolker E, Crapo H. Convex polyhedra, Dirichlet tessellations, and spider webs. In: Senechal M, editor. Shaping space: exploring polyhedra in nature, art, and the geometrical imagination. Springer New York; 2013.
- [10] Zastavni D. The structural design of Maillart's Chiasso Shed (1924): a graphic procedure. Struct Eng Int 2008;18(3):247–52.
- [11] Ochsendorf J, Freeman M. Guastavino vaulting: the art of structural tile. Princeton Architectural Press; 2013, URL https://books.google.com/books?id=-q MngEACAAJ.
- [12] Block P, Van Mele T, Liew A, DeJong M, Escobedo D, Ochsendorf J. Structural design, fabrication and construction of the Armadillo vault. Struct Eng 2018;96(5):10–20.
- [13] Rankine M. Principle of the equilibrium of polyhedral frames. Phil Mag 1864;27(180):92.
- [14] Akbarzadeh M, Van Mele T, Block P. On the equilibrium of funicular polyhedral frames and convex polyhedral force diagrams. Comput Aided Des 2015;63:118–28.
- [15] Akbarzadeh M, Van Mele T, Block P. Spatial compression-only form finding through subdivision of external force polyhedron. In: Proceedings of the international association for shell and spatial structures (IASS) symposium. Amsterdam; 2015
- [16] Akbarzadeh M, Van Mele T, Block P. 3D graphic statics: Geometric construction of global equilibrium. In: Proceedings of the international association for shell and spatial structures (IASS) Symposium. Amsterdam: 2015.
- [17] Nejur A, Akbarzadeh M. Polyframe, efficient computation for 3D graphic statics. Comput Aided Des 2021;134:103003, URL https://www.sciencedirect.com/science/article/pii/S0010448521000142.
- [18] Bolhassani M, Ghomi AT, Nejur A, Furkan M, Bartoli I, Akbarzadeh M. Structural behavior of a cast-in-place funicular polyhedral concrete: Applied 3D graphic statics. In: Proceedings of the international association for shell and spatial structures (IASS) symposium 2018. MIT, Boston, USA; 2018.
- [19] Bolhassani M, Akbarzadeh M, Mahnia M, Taherian R. On structural behavior of a funicular concrete polyhedral frame designed by 3D graphic statics. Structures 2018;14:56–68, URL http://www.sciencedirect.com/science/article/ pii/\$2352012418300079.
- [20] Ghomi AT, Bolhassani M, Nejur A, Akbarzadeh M. The effect of subdivision of force diagrams on the local buckling, load-path and material use of founded forms. In: Proceedings of the international association for shell and spatial structures (IASS) symposium 2018. MIT, Boston, USA; 2018.
- [21] Akbarzadeh M, Bolhassani M, Nejur A, Yost JR, Byrnes C, Schneider J, et al. The design of an ultra-transparent funicular glass structure. In: Structures congress 2019. Orlando, Florida; 2019.
- [22] Akbarzadeh M, Nejur A. PolyFrame: Structural form finding tool using 3D graphic statics. 2017–2019, https://www.food4rhino.com/app/polyframe.
- [23] McNeel R. Rhinoceros: NURBS modeling for windows. Computer software; 2014, URL http://www.rhino3d.com/.

- [24] Jodidio P, Andreu P. Paul andreu: architect. Springer Science & Business Media; 2004.
- [25] Lumb S, Gibbons C, Hale R, Clarke S. Aldar's new headquarters at Al Raha Beach, Abu Dhabi. In: Proceedings of the institution of civil engineers-civil engineering, vol. 162. (6):Thomas Telford Ltd; 2009, p. 51–9.
- [26] Bavunoğlu Z, Güngör C. Transparency in Louvre pyramid and fondation cartier. Glob J Adv Eng Technol Sci 2018.
- [27] Masè S, Cedrola E. Louis Vuitton's art-based strategy to communicate exclusivity and prestige. In: Fashion branding and communication. Springer; 2017, p. 155–84.
- [28] Haldimann M, Luible A, Overend M. Structural use of glass, Vol. 10. Iabse; 2008.
- [29] O'Callaghan J, Bostick C. The apple glass cube: Version 2.0. Chall Glass 2012;3:57–65.
- [30] Henriksen T. Future application of structural use of glass. In: ^(Eds.):Book future application of structural use of glass. IOS Press; 2012, p. 67–70, 2012.
- [31] O'Callaghan J, Marcin M. Thinking big with structural glass. In: Glass performance days. Tampere: Glaston Finland Oy; 2009, p. 59–63.
- [32] Kotz F, Arnold K, Bauer W, Schild D, Keller N, Sachsenheimer K, et al. Three-dimensional printing of transparent fused silica glass. Nature 2017;544(7650):337–9.
- [33] Klein J, Stern M, Franchin G, Kayser M, Inamura C, Dave S, et al. Additive manufacturing of optically transparent glass. 3D Print Additive Manuf 2015;2(3):92–105.
- [34] Nguyen-Van V, Wu C, Vogel F, Zhang G, Nguyen-Xuan H, Tran P. Mechanical performance of fractal-like cementitious lightweight cellular structures: Numerical investigations. Compos Struct 2021;269:114050, URL https://www.sciencedirect.com/science/article/pii/S0263822321005109.
- [35] Nguyen-Van V, Panda B, Zhang G, Nguyen-Xuan H, Tran P. Digital design computing and modelling for 3-D concrete printing. Autom Constr 2021;123:103529, URL https://www.sciencedirect.com/science/article/pii/S0926580520311092.
- [36] Nguyen-Van V, Tran P, Peng C, Pham L, Zhang G, Nguyen-Xuan H. Bioinspired cellular cementitious structures for prefabricated construction: Hybrid design & performance evaluations. Autom Constr 2020;119:103324, URL https://www. sciencedirect.com/science/article/pii/S0026580520309043
- [37] Bos F, Louter C, Veer F. Challenging glass: conference on architectural and structural applications of glass, faculty of architecture, delft university of technology, may 2008. IOS Press; 2008.
- [38] Berezko O. Walkways analysis of "złote tarasy" mall in warsaw. 2013.
- [39] Januszkiewicz K, Banachowicz M. Glass as a component of curvilinear architecture in 21st century. Procedia Eng 2016;161:1490–5.
- [40] Oikonomopoulou F, Veer F, Nijsse R, Baardolf K. A completely transparent, adhesively bonded soda-lime glass block masonry system. J Facade Des Eng 2014;2(3-4):201-21.
- [41] Oikonomopoulou F, Bristogianni T, Barou L, Jacobs E, Frigo G, Veer F, et al. Interlocking cast glass components, exploring a demountable dry-assembly structural glass system. Heron 2018;63(1/2):103–38.
- [42] 3MTM. 3MTM vhbTM structural glazing tape. 2017, https://www.3~m.com/3M/en_US/building-construction-us/applications/structural-glazing-tape.
- [43] DIN 18008-1-glass in building design and construction rules part 1: Terms and general bases. 2019.
- [44] ANSYS. Ansys user manual version 2020. 2020.
- [45] AASHTO. LRFD guide specifications for the design of pedestrian bridges. American Association of State Highway Transportation Officials (AASHTO); 2009.